Angewandte Chemie
Eine Zeitschrift der Gesellschaft Deutscher Chemiker

Supporting Information

Structural Distortion in the Wadsley-Roth Niobium Molybdenum Oxide Phase Triggering Extraordinarily Stable Battery Performance

Z. Wu, G. Liang, W. Kong Pang, J. Zou, W. Zhang, L. Chen, X. Ji, C. Didier, V. K. Peterson, C. U. Segre, B. Johannessen*, Z. Guo**

Experimental Section

Synthesis and structure characterization

Niobium molybdenum oxides were synthesized by a co-precipitation method, followed by annealing at high temperature. The ratios of precursors are set as a Nb/Mo molar ratio equal to 1:1. Typically, 4 mmol $NbCl_5$ (99%, Sigma-Aldrich) and 4 mmol $Na_2MoO_4 \cdot 2H_2O$ (99.5%, Sigma-Aldrich) were dissolved in 20 mL ethanol. After, 20 mL deionized water was added and stirred for another 10 min. Then, the solution was heated at 90 °C in a water bath for 1 h. The resultant blue gel was centrifuged 6 times with ethanol and water alternately. Solids recovered after centrifugation were dried at 60 ℃ in an oven overnight, and then annealed at 900 °C for 18 h with a heating rate of 5 °C min^{-1} in air in a tube furnace. After cooling to room temperature naturally, the powder, named NMO-18h, was collected. In comparison, the NMO-3h powder and the NMO-0.5h powder were prepared by annealing the as-synthesized precursor for 3 h and 0.5 h, respectively.

Thermogravimetric analysis (TGA) was performed on a SETARAM thermogravimetric analyzer (France) with a ramp rate of 5 °C min^{-1} in air. X-ray photoelectron spectroscopy (XPS) was measured by using a VG Multilab 2000 and the binding energies were calibrated by shifting the C 1s peak of the adventitious carbon to 284.8 eV. Inductively Coupled Plasma Optical Emission Spectrometry (ICP-OES) was performed on an Agilent 5110 ICP-OES (Agilent, USA) to determine the atomic ratio of Nb/Mo. The images of the structures and compositions of these samples were examined using field emission scanning electron microscopy (FESEM; JEOL-7500), transmission electron microscopy (TEM; JEOL-2010), and 200 kV probe corrected scanning transmission electron microscopy (STEM; JEOL ARM-200F).

Neutron powder diffraction (NPD) was performed on the high-resolution neutron powder diffractometer Echidna at the Open Pool Australian Light water (OPAL) research reactor at the Australian Nuclear Science and Technology Organisation (ANSTO).[1] High-resolution NPD data of the NMO-18h powder were collected over the 2θ range 4 to 164 ° with a step size of 0.125 ° at the neutron wavelength of 1.62194(4)

Å and 2.44042(7) Å, respectively. The neutron beam wavelength was determined by using the $La^{11}B_6$ National Institute of Standards and Technology (NIST) standard reference material 660b. Joint structural analysis was performed using the GSAS-II software,[2] where the NMO-18h starting structure (ICSD#78034) was refined in an approach involving the refinement of background coefficients, sample displacements, scale factors, lattice parameters, site occupancy factors, isotropic atomic displacement parameters, and atomic positional parameters. The crystalline impurity $NbAlO_4$ (ICSD#82987) was detected at 2.9(1) wt.% as a result of reaction between the precursor and alumina crucible during heat treatment. The schematic crystal structure of NMO-18h was plotted using VESTA.[3]

Electrochemical characterization

The working electrode was made with the active material, super P, and polyvinylidene fluoride (PVDF) in a mass ratio of 8:1:1, respectively. At first, mixed powders (8:1:1) were uniformly dispersed in N-Methyl-2-Pyrrolidone (NMP) using a planetary ball mill. The resultant slurry was coated on copper foil and vacuum-dried in a vacuum oven at 120 °C for 12 h. The dried electrode was then pressed at 30 MPa for 1 min, with a mass loading of active material of ~ 1.2 mg cm^{-2}. CR2032 coin cells were assembled in an argon-filled glove box (O_2 and H_2O level < 0.1 ppm), using metallic Li foil as both counter and reference electrodes, Celgard (product 2400) film as the separator, and 1 M $LiPF_6$ in dimethyl carbonate (DMC) as the electrolyte. The amount of electrolyte used for assembling CR2032 coin cells was about 50 μL per mg of $(Nb, Mo)_{13}O_{33}$. Galvanostatic discharge/charge testing was performed using a Land CT2001A battery testing system over the voltage range 1.0 to 3.0 V in a temperature-controlled room at 25 °C. Cyclic voltammetry (CV) was conducted within the voltage range 1.0 to 3.0 V at a scan rate of 0.1 mV s^{-1} on a Biologic VPM3 electrochemical workstation. GITT measurements were conducted by tracking the voltage evolution after a small current pulse (20 mA g^{-1}) for 10 min and a subsequent rest for 60 min to achieve a steady chemical potential equilibrium within the electrode.

The NCM811|| NMO-18h pouch cells were assembled in dry rooms with dew points below - 40°C. The NCM811 cathode has a size of 30 mm × 42 mm and a mass loading of 7.8 mg/cm^2 while the NMO-18h anode has a size of 30 mm × 42 mm and a mass loading of 8.2 mg/cm^2. The amount of electrolyte was added as 5 g/Ah. Each electrode had the pole lug at the size of 6 mm × 10 mm. Aluminum electrode lugs were welded to the cathodes by an ultrasonic welder while nickel electrode lugs were welded to the anodes by mechanical pressing. NCM811|| NMO-18h pouch cells were tested over the voltage range of 1.0-3.0 V. Each pouch cell was tested under the galvanostatic charge-discharge at 0.5C (1C = 188 mA g^{-1} for NCM811).

In situ synchrotron X-ray powder diffraction

Synchrotron XRD experiments were performed at the powder diffraction beamline at the Australian Synchrotron (Melbourne, Australia), where synchrotron diffraction data was recorded at the wavelength of 0.688800(2) Å at intervals of 10.23 min between acquisitions using a MYTHEN microstrip detector. A customized CR2032 coin-cell was assembled for the *in situ* synchrotron XRD experiment, where holes of diameter 5 mm were punched through both caps to allow the transmission of the synchrotron beam. Aluminum foil was used as the current collector and aluminum conductive tape (3M®) was used to seal the holes on the positive and negative caps to protect against exposure to air. The *in situ* coin cells were cycled at the current density of 30 mA g^{-1} between 1.0 and 3.0 V (*vs.* Li$^+$/Li) with a mass loading of ~ 2 mg cm^{-2}. Sequential refinements were carried out against the *in situ* synchrotron XRD data in the angular range 3.2 to 11.05° using GSAS-II software with the structural model listed in **Table S1**. The background parameters (6 Chebyshev parameters + a peak at 9.6 degrees), sample displacement and overall broadening (W) were determined from the first pattern and fixed in remaining patterns. Indexation of the pattern was straightforward considering the few overlapping reflections in this angular range, with the 010, 002, and 01-2 reflections clearly visible at approximately 3.5°, 5.3°, and 6.1°, respectively. Although heavily overlapped, the group of intense 100, 1-1-1, 1-10, and 10-1 reflections between 9.8 and 10.6° allowed

reliable refinement of the lattice parameter. The unit-cell parameters were refined semi-automatically, by manually setting *a*, *b,* and *c* so that the position of reflections was close to that expected before refining those parameters. Unit-cell parameters α, β, and γ were first set to values in **Table S1** and then allowed to refine, noting high correlation with other unit-cell parameters. The large intensity changes meant that no atomic structure parameters could be refined, and the intensity changes were accounted for by refining a second-order preferred orientation model with spherical harmonics.

In situ synchrotron X-ray absorption spectroscopy

Synchrotron XAS experiments were conducted at the wiggler XAS Beamline (12ID) in Hutch B in Mode 3 at the Australian Synchrotron (Melbourne, Australia) using a Si (311) double-crystal monochromator with a beam slit size of 0.8 × 1.5 mm at ambient temperature in transmission mode. Mo K-edge spectra were recorded at intervals of 17.8 min above and below the absorption edge of 20,000 eV with a Mo foil being measured synchronously as a reference, whilst Nb K-edge spectra were recorded at intervals of 27.8 min above and below the absorption edge of 18,986 eV with a Nb foil used as a reference. The coin-cells used were the same as for the synchrotron XRD measurements, but with a higher electrode mass loading of ~ 10 mg cm^{-2}. To prepare the pellets of Nb_2O_5, NbO_2, MoO_3, MoO_2, NMO-0.5h, NMO-3h, and NMO-18h, the corresponding powder was diluted with cellulose, then well-ground in an agate mortar, and pressed into a pellet of diameter 7 mm to ensure even particle size and homogeneity, thus avoiding distortions to the XAS spectra. The amount of powder used in the pellet was determined by the value where an absorption edge jump equals 1.0. Data normalization, background removal, calibration and alignment, parameter constraint, and peak fitting were performed using the Athena program in the Demeter package running IFEFFIT computation code with standard procedures.[4] The EXAFS spectrum was first converted to k-space, which was then multiplied by k^3 to amplify the oscillations in the upper end of k-space ($k^3\chi(k)$). The k^3-weighted $\chi(k)$ signal was then Fourier transformed with an uncorrected phase shift to provide radial distribution

information. The built-in AUTOBK algorithm was adopted to minimize background below Rbkg = 0.7 Å for Mo K-edge spectra and Rbkg = 1.0 Å for Nb K-edge spectra. The EXAFS data were modeled with the Artemis program using the FEFF8 algorithm. The Mo K-edge spectra were fitted with k, k^2, and k^3 weighting over a k-range from 2 to 9.5 $Å^{-1}$ and an R-range from 0.7 to 2 Å or 0.7 to 3 Å, whilst the Nb K-edge spectra were fitted in k, k^2, and k^3 weighting over a k-range from 2 to 11.5 $Å^{-1}$ and a R-range from 1 to 2 Å or 1 to 4 Å. Major EXAFS parameters such as the coordination distance ($R + \Delta R$), coordination number ($N + \Delta N$), Debye-Waller factor (σ^2), amplitude reduction factor (S_0^2), energy shift (ΔE_0), and R-factor were obtained. All S_0^2 are fixed to 0.91 according to the fit results of the reference Nb and Mo foil. The coordination number was fitted with an error below 25% and the uncertainty of the coordination distance is below 0.02 Å. All R factors are below 2.0%.

Supplementary Figures

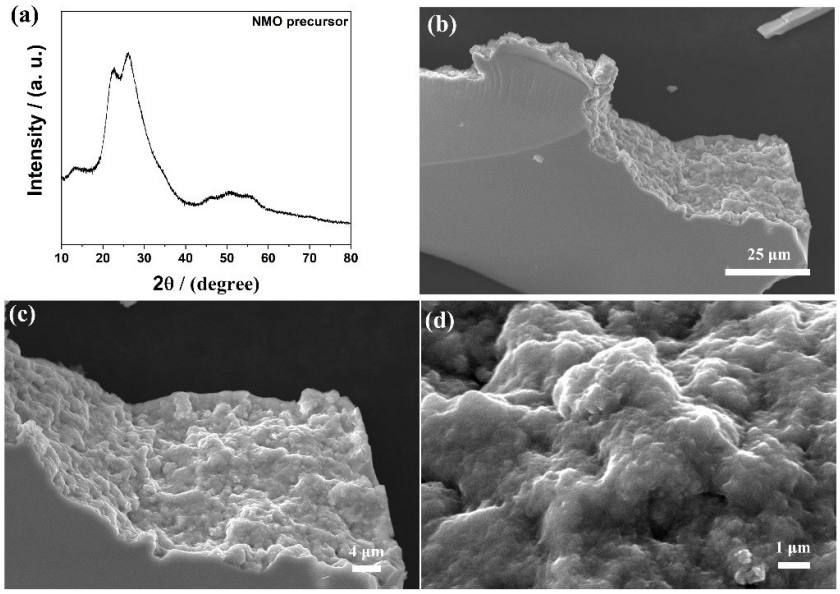

Figure S1 (a) The XRD pattern and (b-d) SEM images of the NMO precursors. It can be obtained that the NMO precursors show large aggregates consisting of nanoparticles with poor crystallinity.

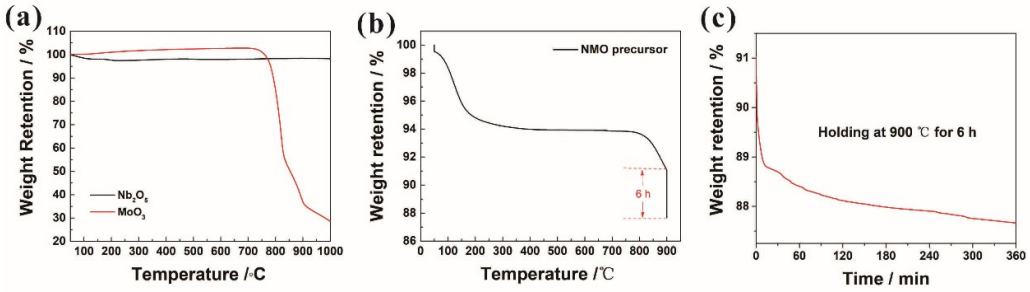

Figure S2 Thermogravimetric analysis of reagents. (a) Commercial Nb_2O_5 and MoO_3 powders heated with a ramp rate of 5 ℃/min in air. (b and c) NMO precursor heated at 5 ℃/min in air to 900 ℃ and held for 6 h.

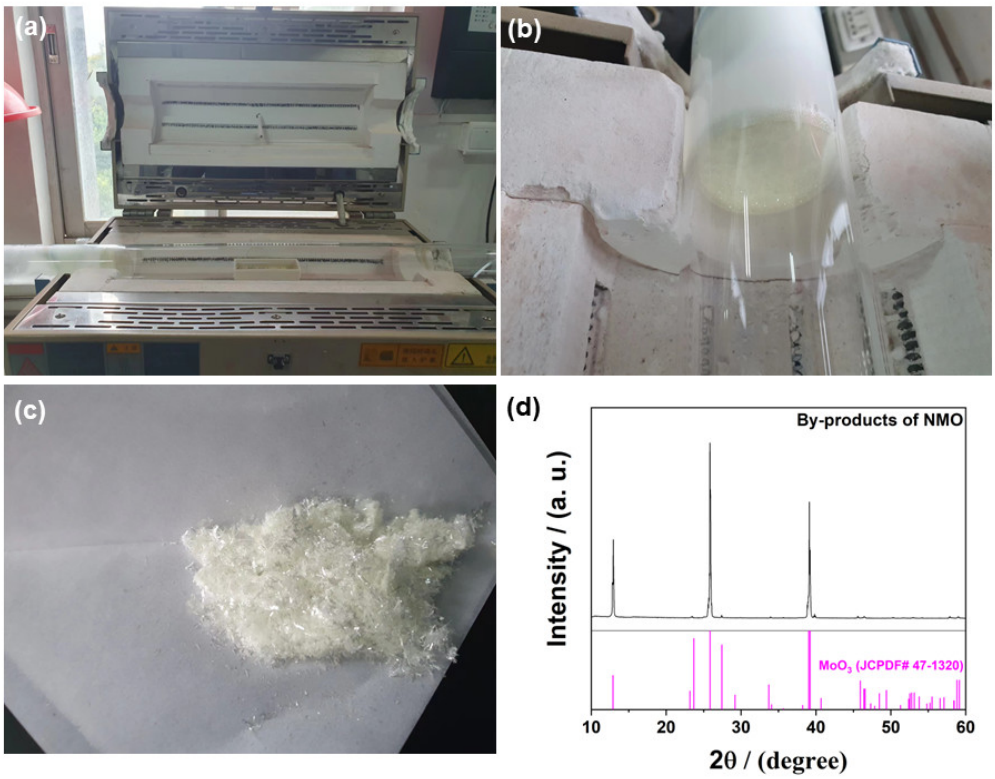

Figure S3 (a-c) Optical images of the by-products in the downstream of the quartz tube after annealing, (d) the corresponding XRD patterns of the MoO_3 by-products.

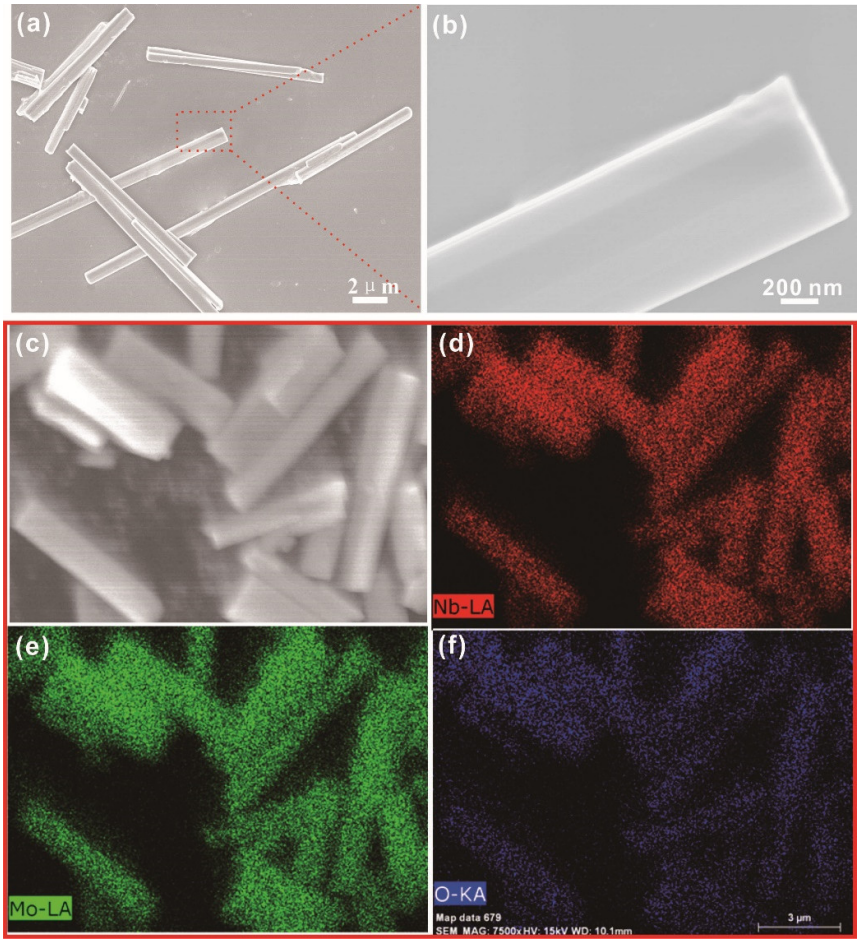

Figure S4 SEM images of the NMO-18h powder and elemental distribution within determined using EDS. The SEM images show bulk cuboids (~1 μm wide and 5 ~ 15 μm long) with preferred orientation growth and the elemental maps show a uniform distribution on the micrometer scale of Nb, Mo, and O element in the cuboids.

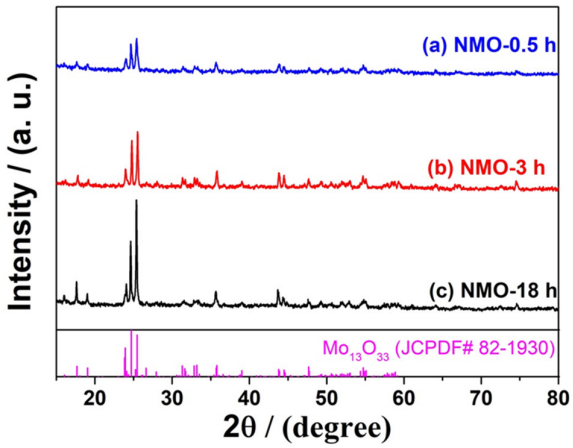

Figure S5 XRD patterns of NMO samples prepared by different annealing time. The peak intensity enhanced with prolonged annealing time, which reveals the decreased disorder degree in the NMO samples. Patterns are shown as a line and offset in y for clarity.

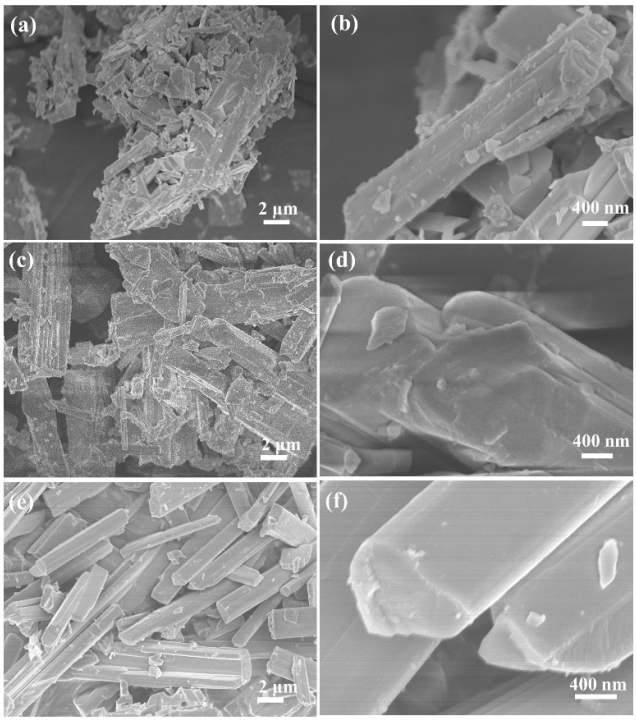

Figure S6 SEM images of (a and b) NMO-0.5h, (c and d) NMO-3h, and (e and f) NMO-18h.

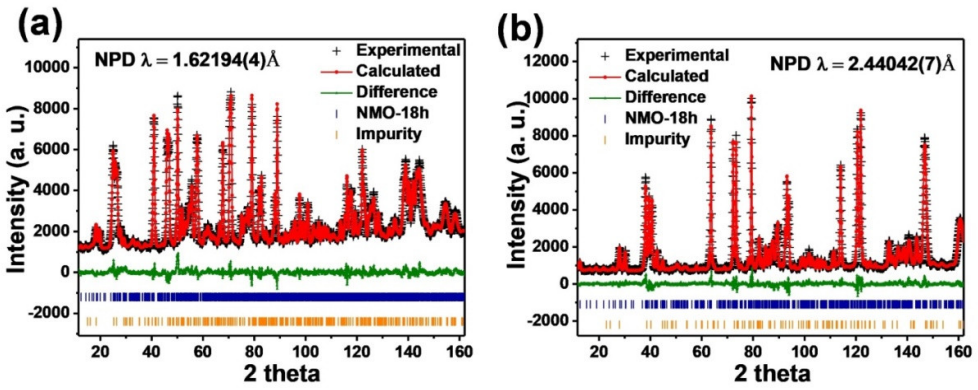

Figure S7 Joint Rietveld refinement profiles using NPD data collected at different wavelengths of the NMO-18h powder (overall weighted profile R-factor R_{wp} = 4.83 % and combined goodness of fit (GOF) = 1.99).

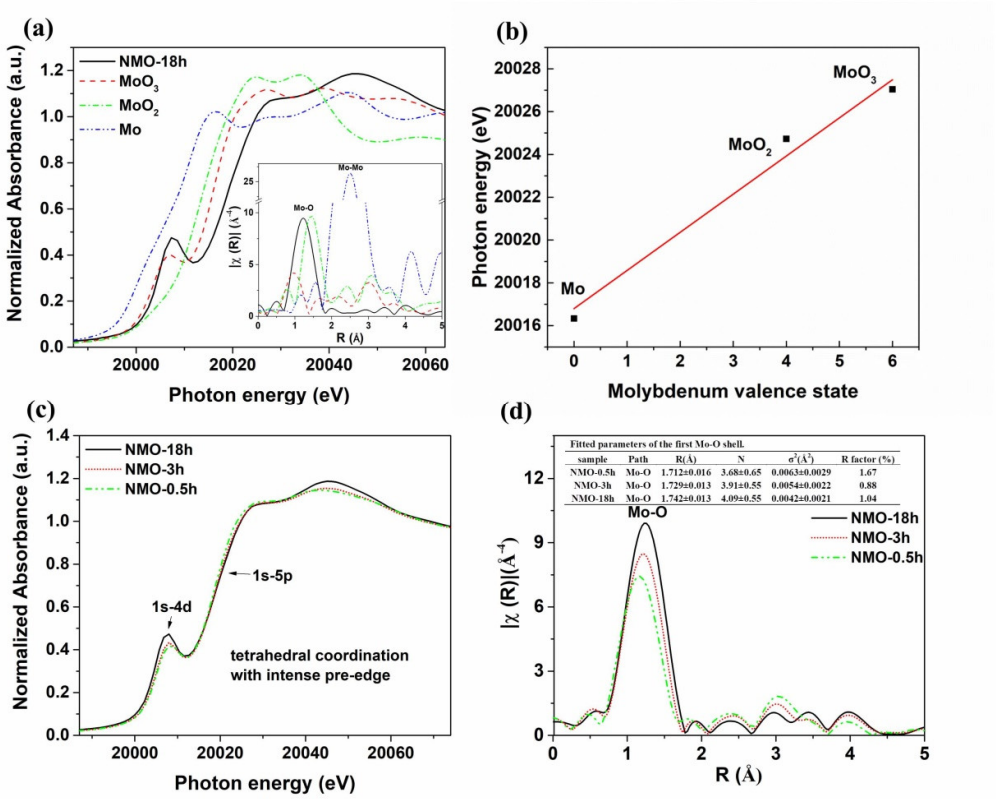

Figure S8 Mo K-edge X-ray absorption spectroscopy and Mo oxidation state of NMO samples and references. (a) XANES data of NMO-18h, MoO_3, MoO_2, and Mo.(b) Calibration of the Mo K-edge white-line peak for $Mo^{VI}O_3$, $Mo^{IV}O_2$, and Mo^0. (c) XANES data of NMO prepared with different annealing time and (d) the corresponding radial structure function obtained by Fourier-transform of the Mo K-edge EXAFS oscillations. The fitted structural parameters of the first Mo-O shell for NMO samples are shown inset in Figure S4d, showing increased Mo-O coordination number and bond length, as well as decreased Debye-Waller factor on increased annealing time. Further, dampening of the peak at around 3 Å is shown.

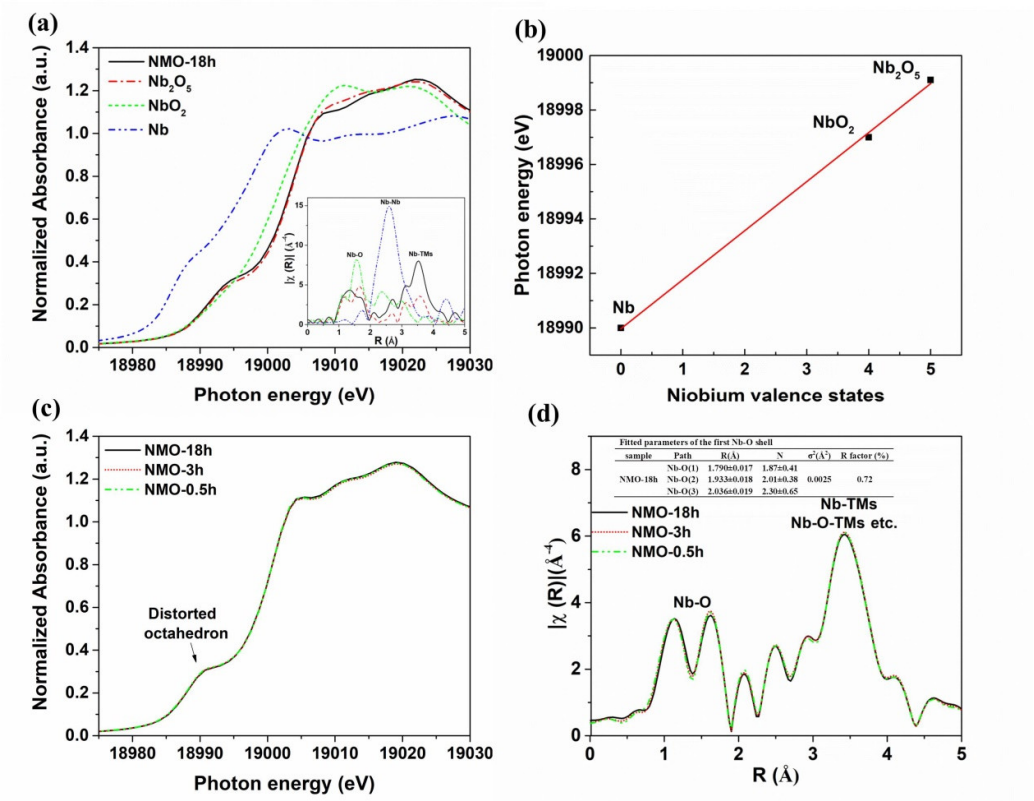

Figure S9 Nb K-edge X-ray absorption spectroscopy and Nb oxidation states for NMO samples and references. (a) XANES spectra of NMO-18h, Nb_2O_5, NbO_2 and Nb. (b) Calibration of Nb K-edge at E(0.5) for $Nb^{V}{}_2O_5$, $Nb^{IV}O_2$ and Nb^0. (c) XANES spectra of NMO samples prepared with different annealing times and (d) the corresponding radial structure function obtained by FT of the Nb K-edge EXAFS oscillations and the fitted structural parameters of the first Nb-O shell for the NMO-18h powder (inset).

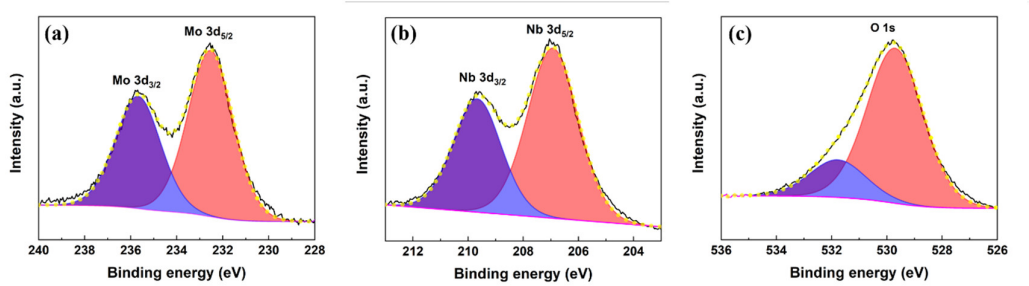

Figure S10 High-resolution X-ray photoelectron spectroscopy data of NMO-18h powder in the (a) Mo 3d region, (b) Nb 3d region, and (c) O 1s region. The doublet at 232.7 and 235.9 eV can be assigned to the Mo 3d5/2 and Mo 3d3/2 orbital electrons of tetrahedral Mo(VI), whilst the doublet at 207.1 and 209.8 eV can be assigned to the Nb 3d5/2 and Nb 3d3/2 orbital electrons of Nb(V), whilst the doublet at 529.7 and 531.8 eV can be assigned to the O 1s orbital electrons of metal oxides and adventitious contamination, respectively.[5] Data are shown as a black line, with components in purple and red, and their total as the yellow line.

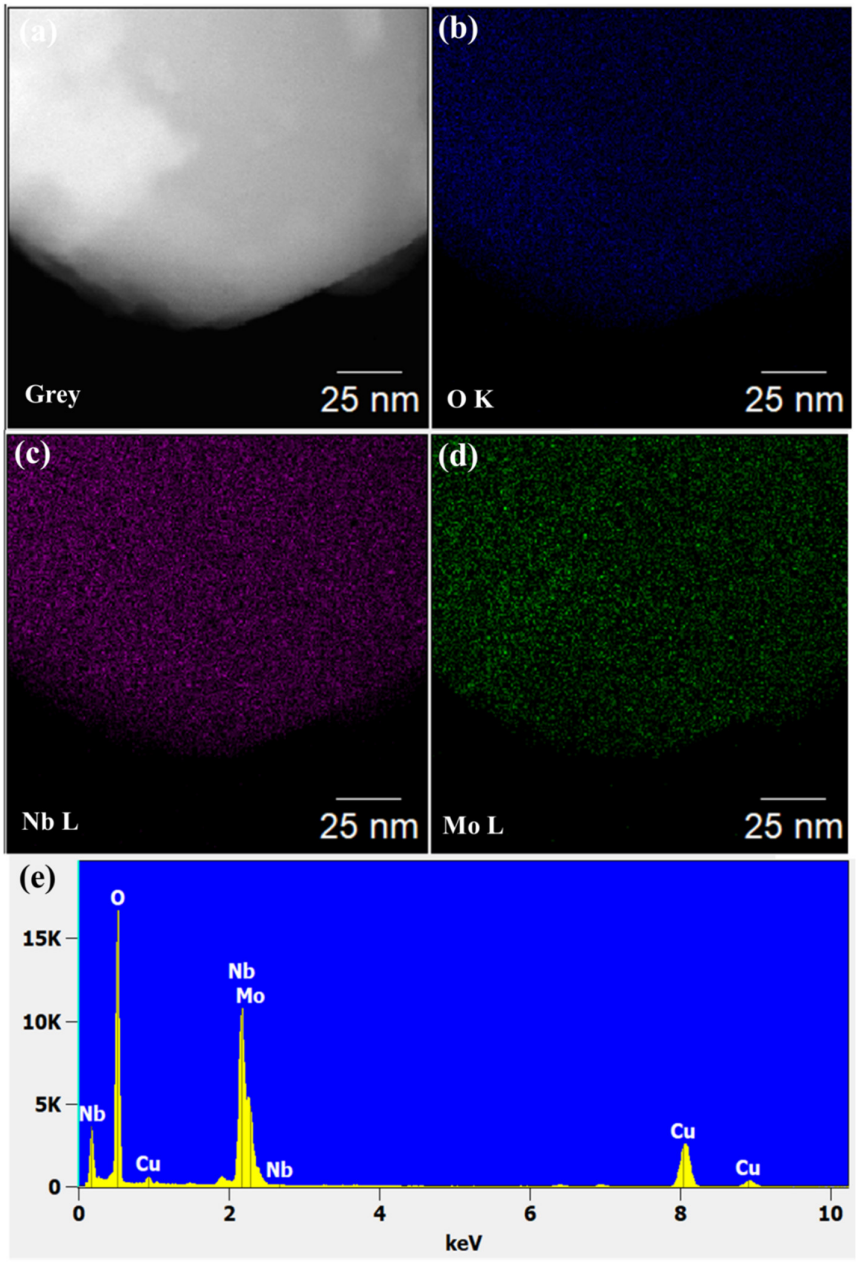

Figure S11 STEM-EDS elemental analysis of the NMO-18h powder shown as (a-d) maps, and (e) a spectrum.

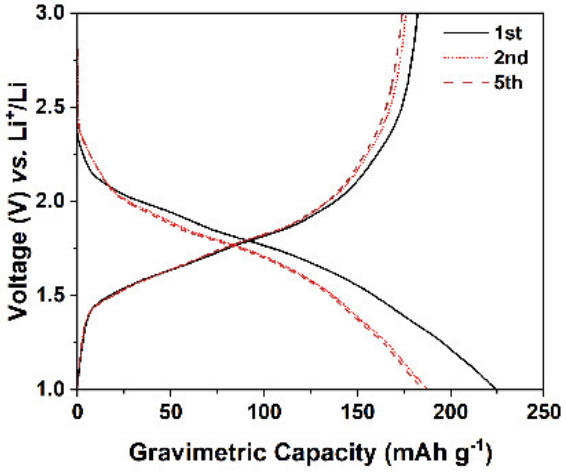

Figure S12 The charging/discharging curves of the NMO-18h electrode during the initial 5 cycles at a current density of 20 mA/g.

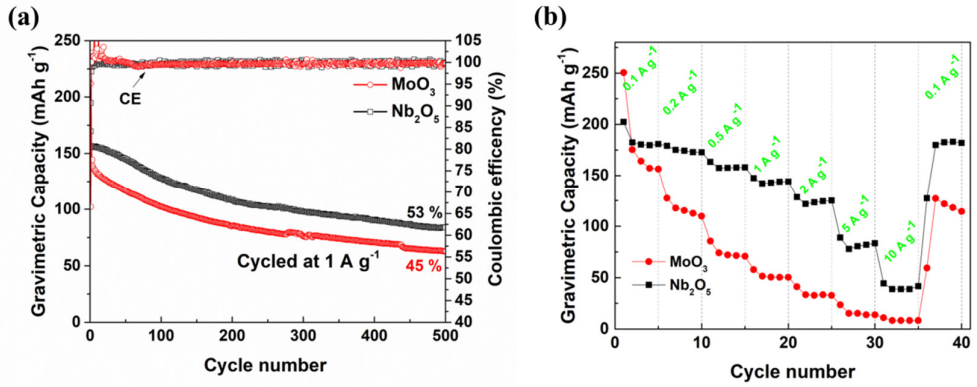

Figure S13 Electrochemical performance of LIBs with commercial MoO_3 and Nb_2O_5 anodes. (a) Cycling stability at 1 A g^{-1} and (b) rate performance of LIBs from 0.1 A g^{-1} to 10 A g^{-1}. CE = coulombic efficiency.

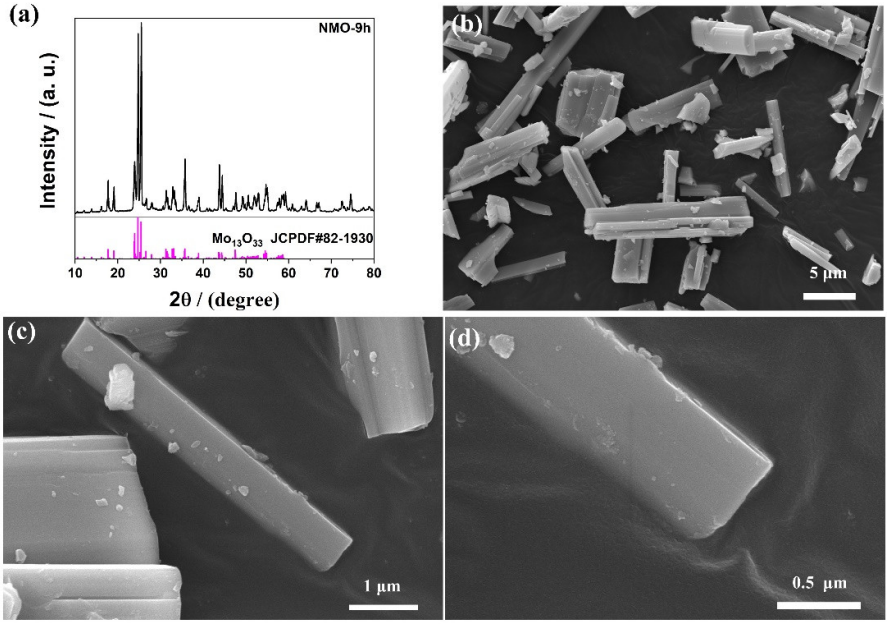

Figure S14 (a) The XRD pattern and (b-d) SEM images of the NMO-9h.

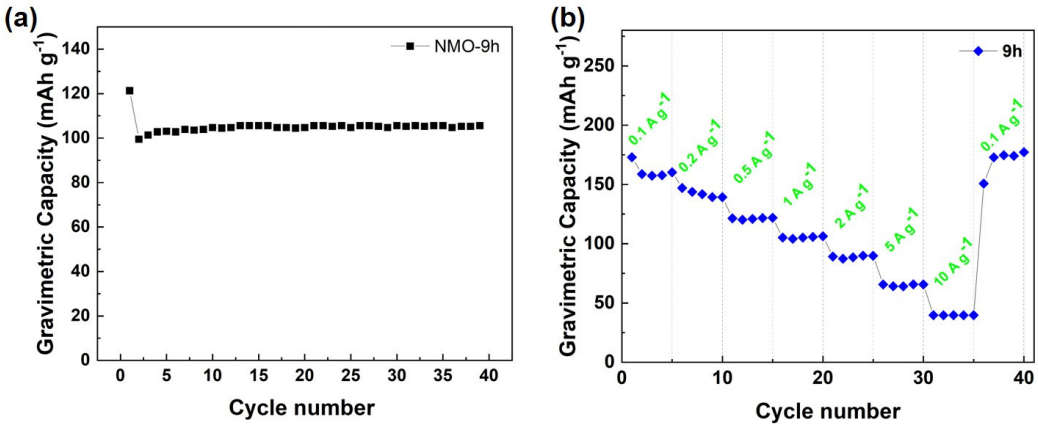

Figure S15 (a) Cycling performance at 1 A g^{-1} for the NMO-9h electrode and (b) rate performance of the NMO-9h electrode measured from 0.1 to 10 A g^{-1}.

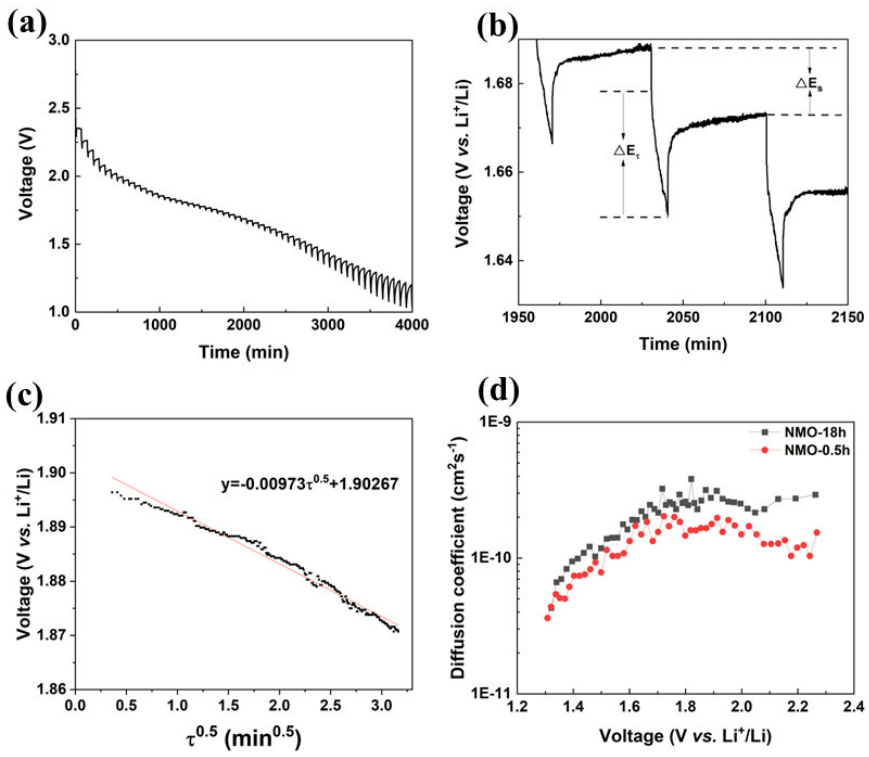

Figure S16 GITT tests of the NMO-18h and NMO-0.5h electrode. (a) GITT discharge curve of the NMO-18h electrode (after activation for 5 cycles) tested at 20 mA g^{-1}. (b) Voltage as a function of discharge time for a single step of the NMO-18h electrode. (c) Linear relationship of the voltage versus $\tau^{0.5}$ during a typical titration with fit shown in red. (d) Calculated Li^+ diffusion coefficient of the NMO-18h and NMO-0.5h electrode. Lines through the points are a guide only.

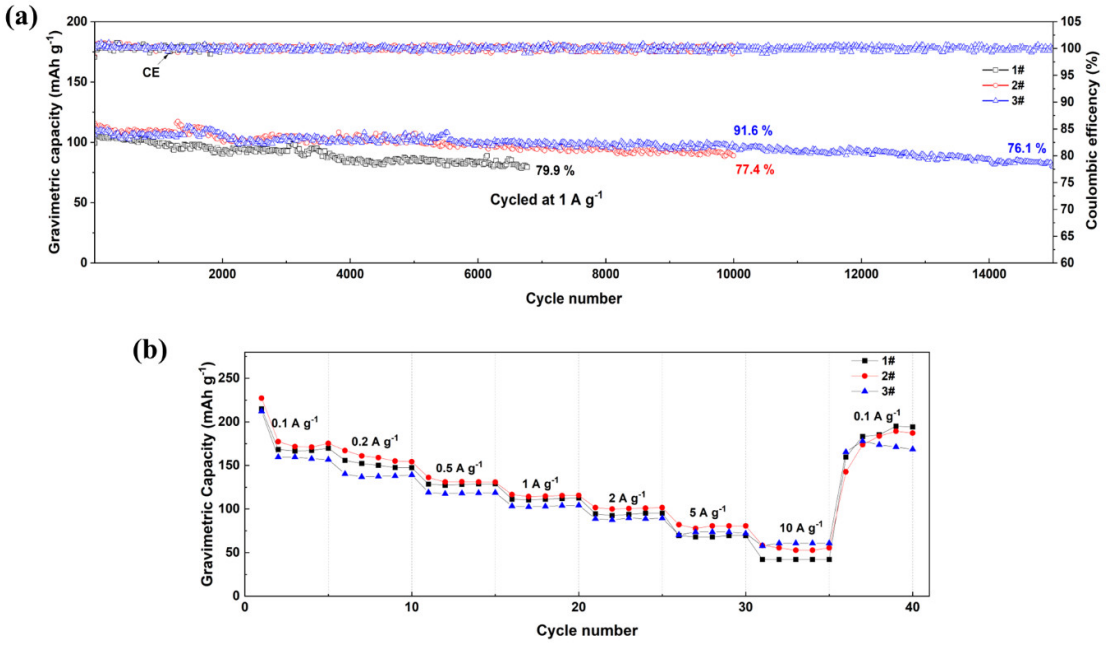

Figure S17 (a) Cyclic performance and (b) rate performance of multiple cells for the NMO-18h electrode. Note that the 2# cell runs for only 10000 cycles as it ceases for recording data due to the cyclic termination of the procedure while 3# cell loses the follow-up data due to shutdown of the electric power. Despite these objective factors, the good rate and cyclic performance were reproducible even in different cells with similar material compositions (NMO-18h-B).

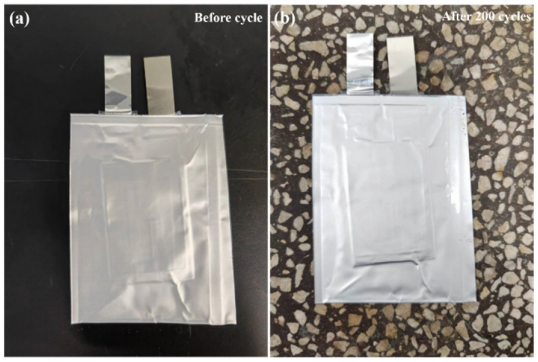

Figure S18 Optical images of the (Nb, Mo)13O33 containing pouch cell before and after 200 charge/discharge cycles.

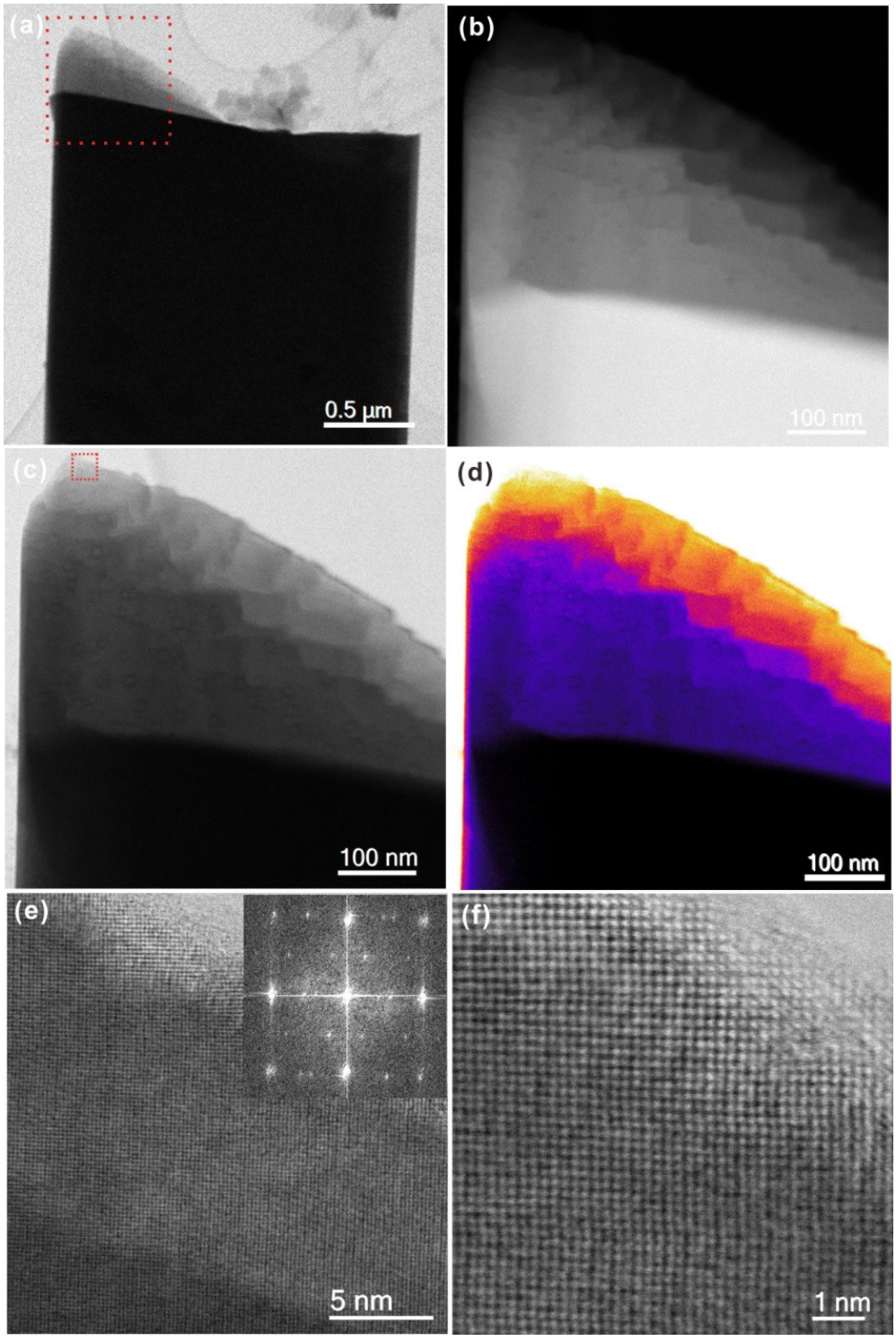

Figure S19 STEM images of the *ex situ* NMO-18h electrode upon full discharge. (a, c, e and f) Bright-field STEM images at different magnifications, (b) the HAADF-STEM image, and (d) the colored bright-field STEM image of the *ex situ* electrode upon full discharge.

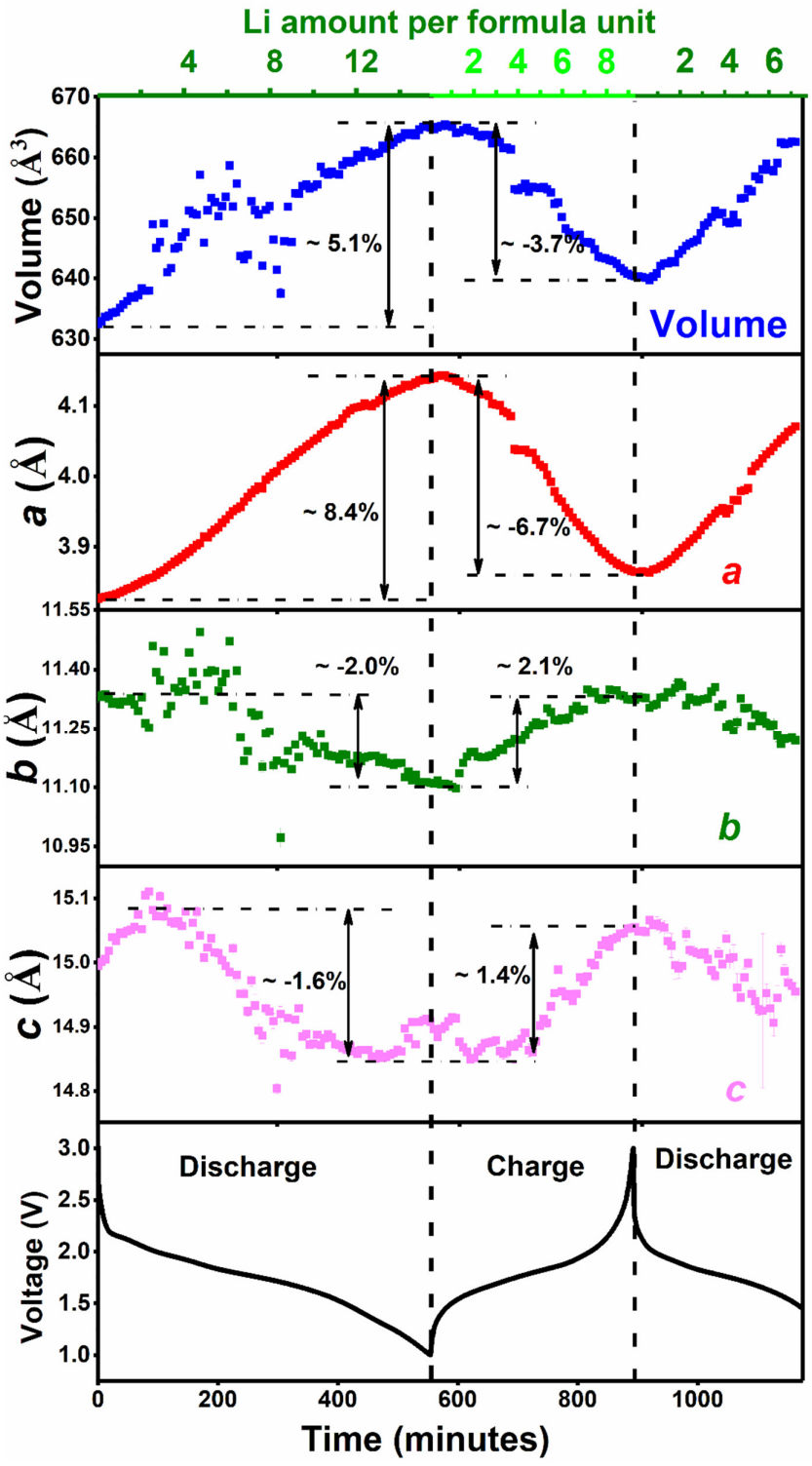

Figure S20 Sequential refinement results for NMO-18h against *in situ* synchrotron XRD data, including the evolution of lattice parameters and cell volume. The corresponding electrochemical curve and Li concentration per formula unit are shown at the bottom and top, respectively. Errors are shown smaller than the points.

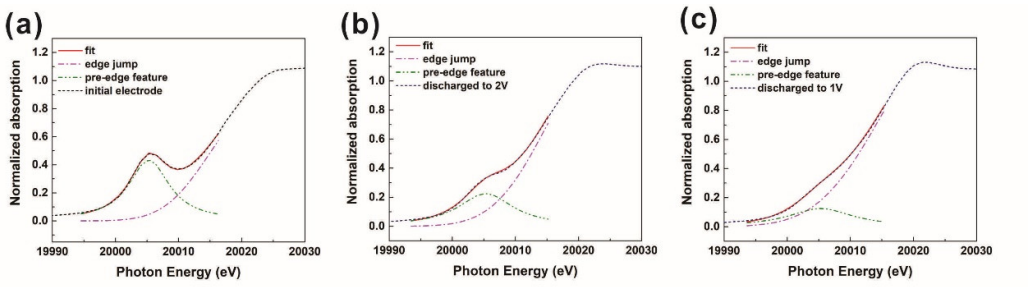

Figure S21 Mo K-edge X-ray absorption pre-edge feature of the *in situ* NMO-18h electrode fitted by a Levenberg-Marquardt non-linear least-squares minimization. Example fits are shown for the *in situ* electrode data at approximately (a) 3.0 V, (b) 2.0 V, and (c) 1.0 V. Data were fitted by an edge jump model with a sigmoidal error function and a Lorentzian pre-edge peak.

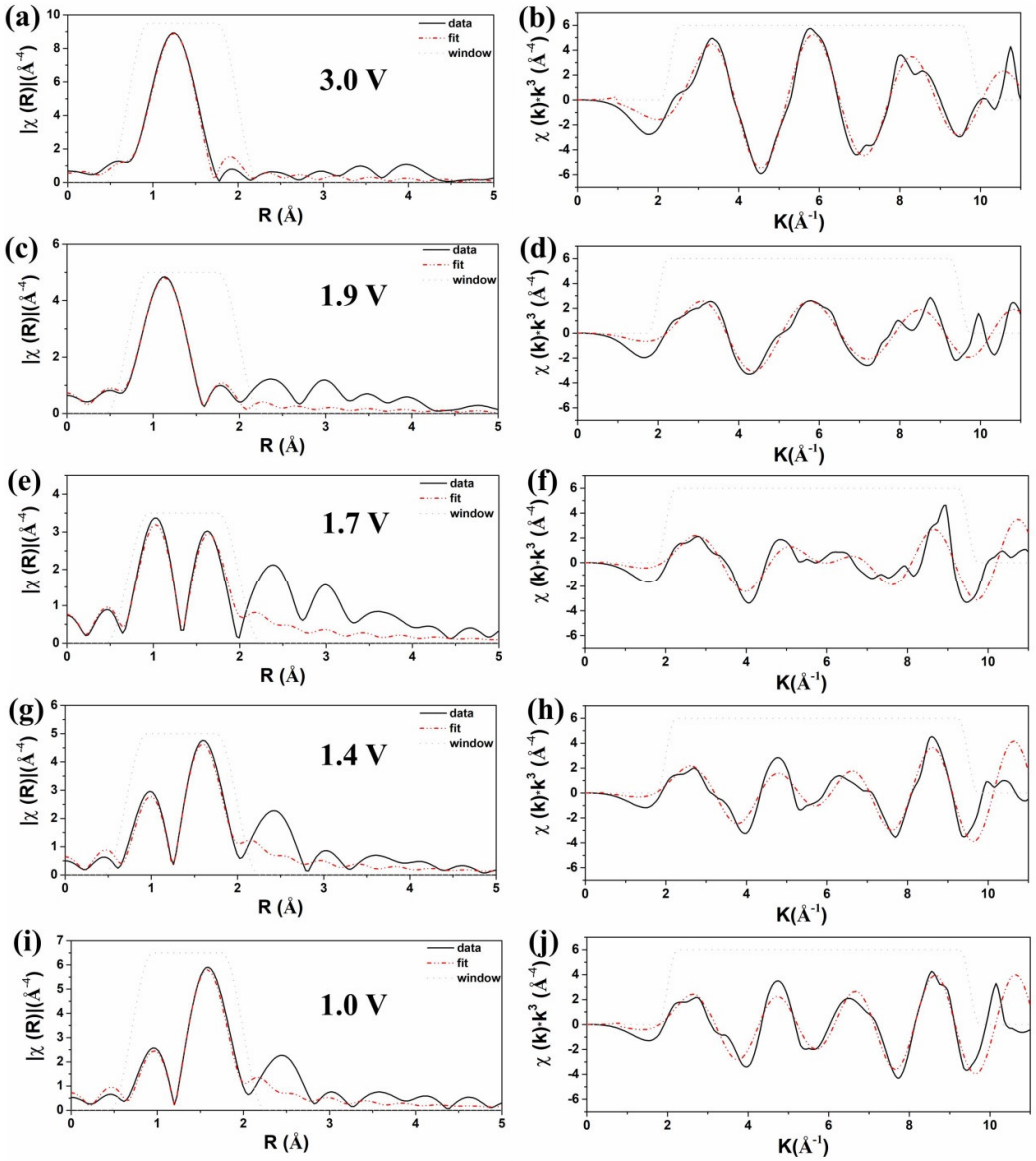

Figure S22 Fits of *in situ* Mo K-edge EXAFS spectra of the NMO-18h electrode. Example fits of both R-space and k-space are shown for the electrode at (a, b) 3.0 V, 0 mAh g^{-1} (c, d) 1.9 V, 50 mAh g^{-1} (e, f) 1.7 V, 100 mAh g^{-1} (g, h) 1.4 V, 150 mAh g^{-1} and (i, j) 1.0 V, 210 mAh g^{-1}. (R ranges from 0.7 to 2 Å; k ranges from 2 to 9.5)

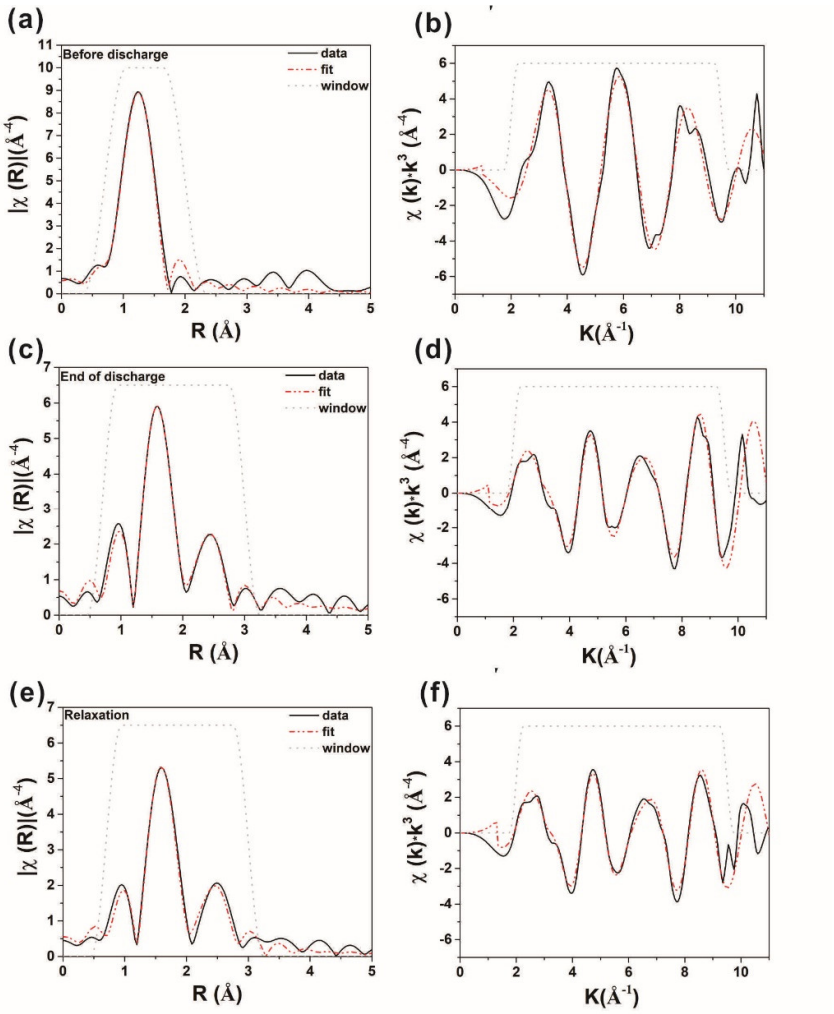

Figure S23 Fits of Mo K-edge EXAFS data of the *in situ* NMO-18h electrode under different states. Radical radial distribution functions and Mo K-edge EXAFS oscillation fits (a and b) before discharge, (c and d) at the end of discharge, and (e and f) under open circuit with relaxation. (R ranges from 0.7 to 2 Å or 0.7 to 3 Å; k ranges from 2 to 9.5)

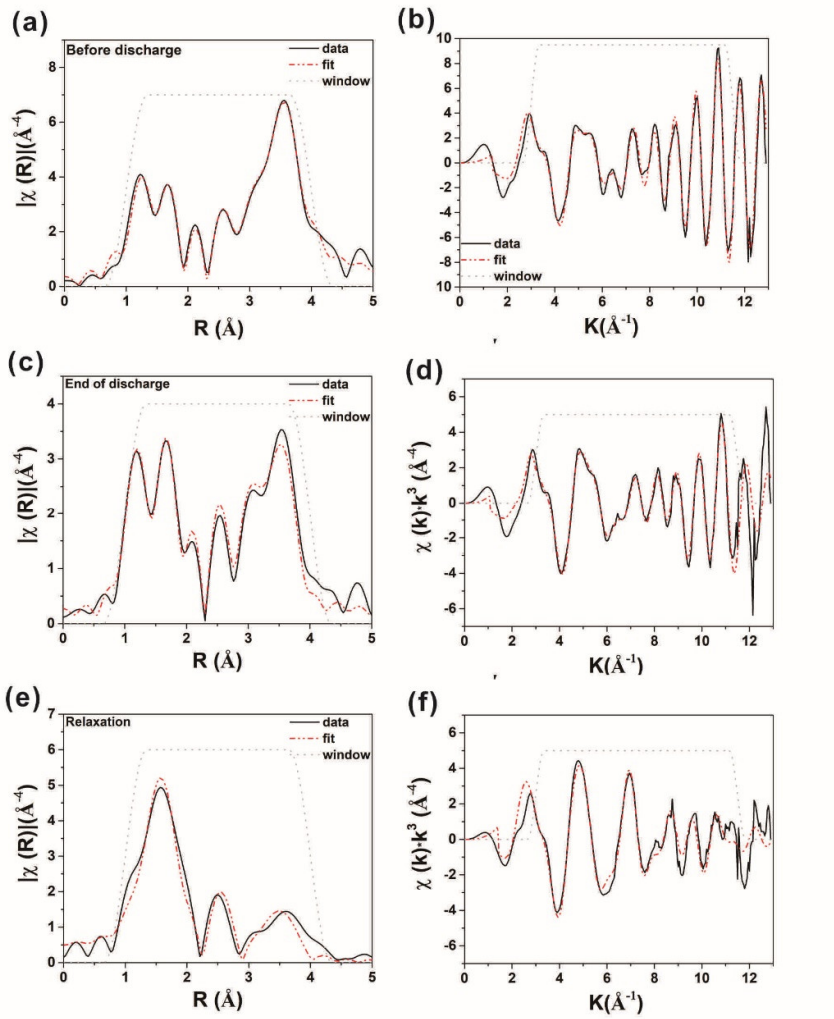

Figure S24 Model fits to *in situ* Nb K-edge EXAFS data of the NMO-18h electrode under different states. Radical radial distribution function and Nb K-edge EXAFS oscillation fits (a and b) before discharge, (c and d) at the end of discharge, and (e and f) under open circuit with relaxation. (R ranges from 1 to 4 Å; k ranges from 3 to 11.5)

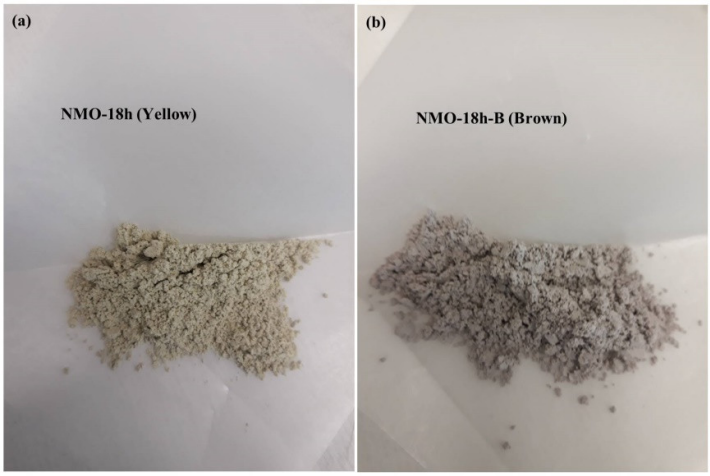

Figure S25 Photographs of yellow NMO-18h powder (prepared at 900 ℃ for 18 h with an initial Nb/Mo atomic ratio of 1) and brown NMO-18h-B powder (prepared at 900 ℃ for 18 h using an initial Nb/Mo atomic ratio of 9/4).

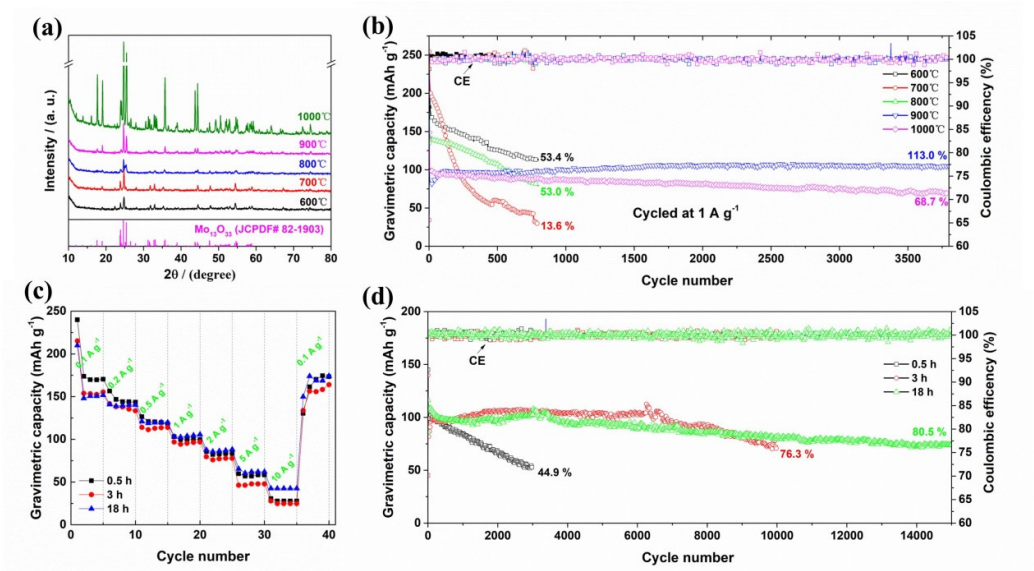

Figure S26 XRD data and electrochemical properties of other NMO electrodes for LIBs. (a) XRD data of NMO powders annealed at different temperatures for 3 h using an initial Nb/Mo atomic ratio of 9/4 (data are offset in y for clarity) and (b) their corresponding cycling performance measured at 1 A g^{-1}. (c) Rate performance measured from 0.1 to 10 A g^{-1} and (d) cycling performance evaluated at 1 A g^{-1} for NMO powders prepared by annealing at 900 ℃ for 0.5 h, 3h, and 18 h, respectively, using an initial Nb/Mo atomic ratio of 9/4.

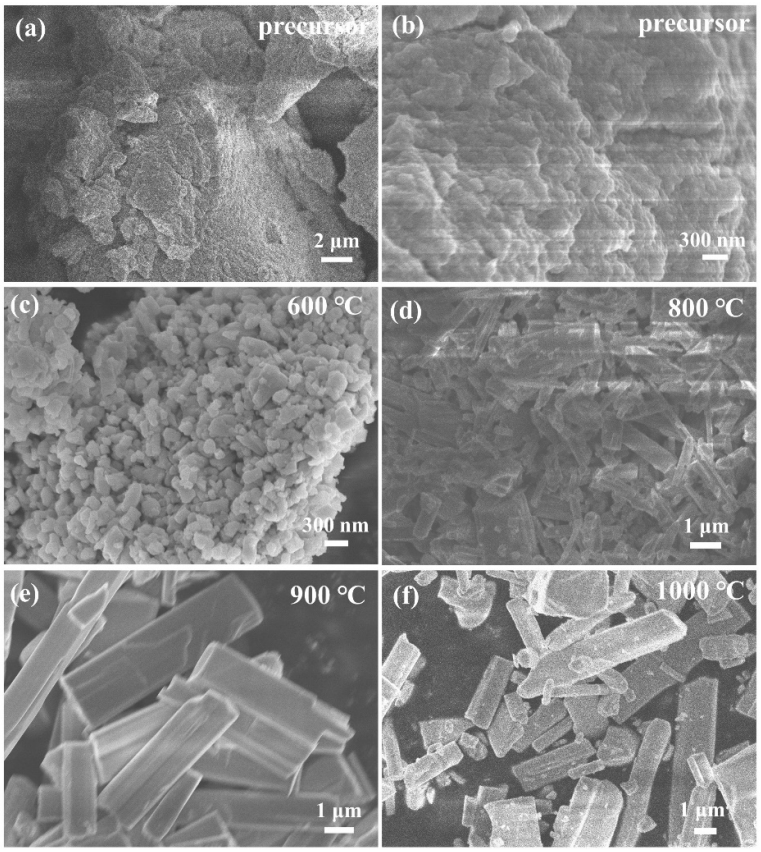

Figure S27 SEM images of other NMOs (a and b) precursors, (c-f) prepared at 600℃, 800℃, 900℃,1000℃, respectively, for 3 hours using an initial Nb/Mo atomic ratio of 9/4.

With the increasing annealing temperature for NMO precursors, the morphology of NMO changes from nanoparticles (600 ℃), mixed particles/ cuboids (800 ℃), to micro-levelled cuboids (900 ℃, 1000 ℃). Although the morphology of NMO prepared at 1000 ℃ is micro-levelled cuboids which are similar with NMO prepared at 900℃, the cycling stability becomes worse when the annealing temperature increases from 900 to 1000 ℃. At 900 ℃, the NMO-B electrode shows the best cycling stability, which is better than nanoparticles (600 ℃) and micro-levelled cuboids 1000 ℃, revealing that the grain size and the morphology may impact the performance but could not determine the cycling stability of NMO.

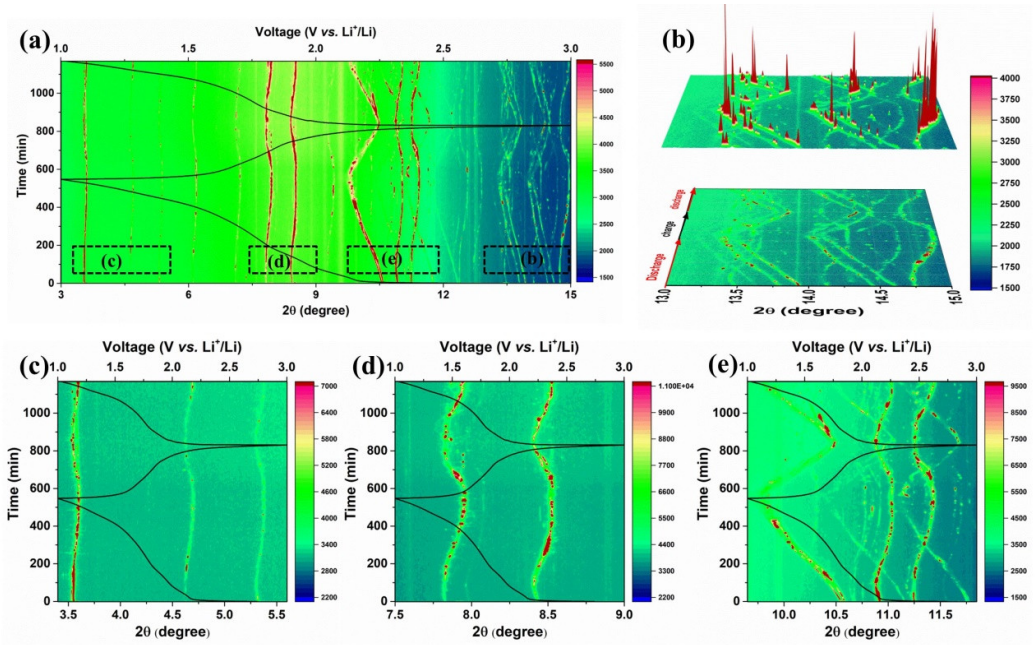

Figure S28 Time-resolved *in situ* synchrotron XRD data of the NMO-18h-B electrode superimposed with the electrochemical curve. (a) A full view and (c-e) selected 2θ region of the *in situ* data shown as 2D contour plots with intensity in color. (b) A selected 2θ region shown as 3D colormap surface with projection.

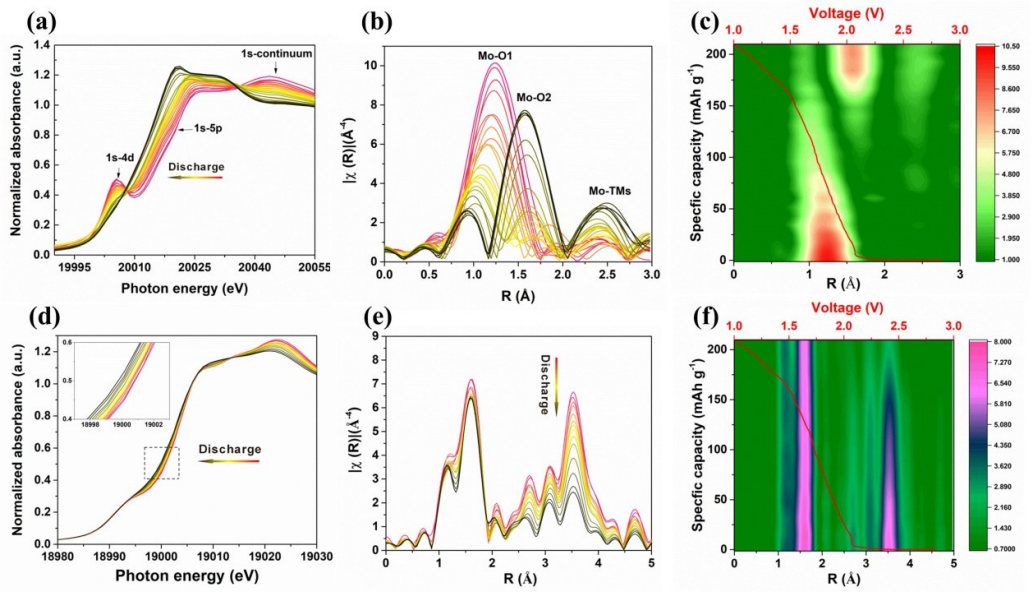

Figure S29 Time-resolved *in situ* (a-c) Mo K-edge and (d-f) Nb K-edge XAS data of the NMO-18h-B electrode during initial discharge. (a and d) *In situ* XANES data; (b and e) FTs of the corresponding k^3-weighted EXAFS data; (c and f) FTs of the corresponding k^3-weighted EXAFS data shown as a 2D contour plot with superimposed electrochemical curve.

Supplementary Tables

Table S1 Crystallographic details of the NMO-18h sample obtained from joint Rietveld refinement.

Starting structure	**$Nb_{12}MoO_{33}$ (ICSD#78034)**		**Impurity ($NbAlO_4$, ICSD#82987)**		
Weight ratio (%)	**97.1(1)**		**2.9(1)**		
$Nb_{12}MoO_{33}$ **Space group: $P\bar{1}$ Unit cell volume: 631.71(2) Å^3** **a = 3.8245(1) Å, b = 11.3104(5) Å, c = 15.010(1) Å** **α = 94.049(7) °, β = 97.378(2) °, γ = 99.7899(4) °**					
Atom	***x***	***y***	***z***	**U_{iso}**	**Site occupancy factor**
Nb/Mo	0.951(4)	0.0469(9)	0.8842(5)	0.0069(3)	Nb : Mo = 0.91 : 0.09 [a, b]
	0.178(5)	0.3765(7)	0.9728(6)		
	0.256(5)	0.2870(7)	0.2162(5)		
	0.111(5)	0.8561(7)	0.3638(5)		
	0.317(5)	0.1857(6)	0.4535(4)		
	0.107(4)	0.4709(6)	0.7312(5)		
Mo	0.252(3)	0.500(2)	0.498(1)		0.52(1)
O	0.450(5)	0.0436(8)	0.8689(6)	0.0052(2)	1[a]
	0.246(4)	0.0250(9)	0.4208(6)		
	0.143(6)	0.4353(8)	0.8486(6)		
	0.075(5)	0.5322(7)	0.5983(5)		
	0.003(6)	0.6873(8)	0.3214(6)		
	0.307(5)	0.2480(9)	0.3465(6)		
	0.102(3)	0.8961(8)	0.2494(6)		
	0.078(5)	0.2278(8)	0.9230(7)		
	0.225(6)	0.6729(7)	0.7708(5)		
	0.229(7)	0.3385(9)	0.0966(7)		
	0.171(5)	0.1234(9)	0.1736(7)		
	0.380(6)	0.1568(8)	0.6032(5)		
	0	0	0		
	0.433(5)	0.3672(7)	0.5126(6)		
	0.148(5)	0.8113(7)	0.5091(6)		
	0.367(6)	0.4783(8)	0.2728(6)		
	0.301(6)	0.5751(9)	0.0190(6)		

[a] The site occupancy factor is constrained to be 1.

[b] The site occupancy factor is fixed to that obtained from ICP-OES.

Table S2 Metal - oxygen bond lengths in NMO-18h obtained from joint Rietveld refinement (bond length in Å)

	1-Nb/Mo (Octahedra site)	2-Nb/Mo (Octahedra site)	3-Nb/Mo (Octahedra site)	4-Nb/Mo (Octahedra site)	5-Nb/Mo (Octahedra site)	6-Nb/Mo (Octahedra site)	7-Mo (Tetrahedra site)
O1	**1.890(27)**	**2.012(13)**	**2.021(13)**	**1.981(10)**	**1.820(10)**	**1.820(8)**	**1.72(4)**
O2	**1.961(27)**	**1.733(10)**	**1.986(25)**	**1.924(9)**	**1.795(9)**	**2.166(8)**	**1.79(4)**
O3	**2.146(10)**	**1.939(13)**	**1.952(25)**	**1.814(10)**	**2.282(8)**	**1.876(9)**	**1.76(4)**
O4	**2.046(9)**	**2.264(10)**	**1.926(13)**	**1.974(24)**	**2.131(8)**	**2.262(8)**	**1.82(4)**
O5	**2.018(11)**	**1.996(25)**	**1.877(11)**	**1.989(24)**	**1.975(22)**	**2.034(25)**	**N/A**
O6	**1.844(3)**	**1.983(25)**	**2.208(10)**	**2.260(9)**	**2.008(22)**	**1.958(25)**	**N/A**

The shortest and longest bond lengths in specific octahedra are highlighted in green and red, respectively.

Table S3 Comparison of the cycle lifespan, rate capability, and lithium diffusivity rate of NMO-18h with other reported state-of-the-art materials.

Materials	**Cycle lifespan (cycles)**	**Rate Capability**	**Li^+ diffusivity rate ($cm^2\ s^{-1}$)**	**Referenced work**
NMO-18h	15000	60 mAh g^{-1} at 10 A g^{-1} (53.2 C)	10^{-11}~10^{-10}	This work
$Nb_{14}W_3O_{44}$	1000	57.7 mAh g^{-1} at 17.8 A g^{-1} (100 C)	10^{-12}~10^{-10}	Adv. Mater. 2020, 32, 1905295
$Nb_{18}W_{16}O_{93}$	1000	105 mAh g^{-1} at 10.3 A g^{-1} (100 C)	10^{-13}~10^{-12}	Nature 2018, 559(7715): 556-563
$FeNb_{11}O_{29}$	10000	75 mAh g^{-1} at 10.4 A g^{-1} (50 C)	/	Nano Lett. 2021, 21, 9675−9683
$MoNb_{12}O_{33}$	1000	138 mAh g^{-1} at 10 C	10^{-15}~10^{-13}	J. Mater. Chem. A, 2019,7, 6522-6532
$MoNb_6O_{18}$	60	~50 mAh g^{-1} at 5 C	10^{-10}	Mater. Adv., 2021, 2, 6272-6277
$Nb_{14}Mo_3O_{44}$	500	74 mAh g^{-1} at 5 C	10^{-16}~10^{-15}	J Alloy. Compound., 2021, 864, 158379
Nb_2O_5	100	85 mAh g^{-1} at 12.1 A g^{-1} (60C)	/	J. Am. Chem. Soc.2016, 138, 8888−889
Nb_2O_5 / Graphene	10000	75 mAh g^{-1} at 100 C	/	Science, 2017, 356, 599-604
Nb_2O_{5-x}	4000	130 mAh g^{-1} at 100 C	10^{-12}	iScience 2020, 23, 100767
$Nb_9W_4Ti_4O_{42.5}$	7500	138 mAh g^{-1} at 6 A g^{-1} (30 C)	10^{-15}~10^{-12}	Energy Environ. Sci. 2023, 16, 241-251
$Li_4Ti_5O_{12}$ / Graphene	4000	123 mAh g^{-1} at 100 C	10^{-11}	Energy Storage Mater. 2020, 27, 387-395

Note that the value of 1C was defined 188 mA g^{-1}.

Table S4 Structural parameters of the first Mo-O shell from *in situ* Mo K-edge EXAFS data.

sample	Path	R (Å)	N	$\sigma^2\times10^{-3}$ (Å^2)	R factor (%)
1	Mo-$O_{(1)}$	1.75±0.01	4.1±0.2	6±1	0.59
2	Mo-$O_{(1)}$	1.75±0.01	3.9±0.2	6±1	0.65
3	Mo-$O_{(1)}$	1.74±0.01	3.6±0.1	6±1	0.39
4	Mo-$O_{(1)}$	1.73±0.01	3.4±0.1	6±1	0.59
5	Mo-$O_{(1)}$	1.73±0.01	3.2±0.1	6±1	0.35
6	Mo-$O_{(1)}$	1.72±0.01	3.0±0.2	6±1	0.87
7	Mo-$O_{(1)}$ Mo-$O_{(2)}$	1.72±0.01 1.95±0.02	2.8±0.1 1.2±0.2	5±1	0.12
8	Mo-$O_{(1)}$ Mo-$O_{(2)}$	1.72±0.01 1.94±0.02	2.7±0.2 1.7±0.3	5±1	0.40
9	Mo-$O_{(1)}$ Mo-$O_{(2)}$	1.70±0.01 1.92±0.01	2.5±0.2 2.0±0.2	4±1	0.54
10	Mo-$O_{(1)}$ Mo-$O_{(2)}$	1.70±0.02 1.93±0.02	2.3±0.2 2.0±0.3	4±1	0.89
11	Mo-$O_{(1)}$ Mo-$O_{(2)}$	1.72±0.02 1.96±0.02	2.2±0.2 2.4±0.3	3±1	0.75
12	Mo-$O_{(1)}$ Mo-$O_{(2)}$	1.73±0.02 1.97±0.02	2.2±0.2 2.8±0.3	4±1	0.80
13	Mo-$O_{(1)}$ Mo-$O_{(2)}$	1.74±0.01 1.99±0.01	2.1±0.2 2.9±0.2	3±1	0.68
14	Mo-$O_{(1)}$ Mo-$O_{(2)}$	1.75±0.01 1.99±0.01	2.0±0.2 3.3±0.2	4±1	0.51
15	Mo-$O_{(1)}$ Mo-$O_{(2)}$	1.75±0.02 2.00±0.02	2.0±0.3 3.3±0.3	4±1	0.87
16	Mo-$O_{(1)}$ Mo-$O_{(2)}$	1.76±0.02 2.01±0.02	1.8±0.3 3.3±0.3	4±1	0.85
17	Mo-$O_{(1)}$ Mo-$O_{(2)}$	1.75±0.01 2.00±0.01	1.7±0.2 3.5±0.2	4±1	0.49
18	Mo-$O_{(1)}$ Mo-$O_{(2)}$	1.74±0.01 2.00±0.01	1.8±0.3 3.8±0.3	4±1	0.51
19	Mo-$O_{(1)}$ Mo-$O_{(2)}$	1.75±0.01 2.01±0.01	2.0±0.4 3.9±0.3	3±1	0.80
20	Mo-$O_{(1)}$ Mo-$O_{(2)}$	1.74±0.01 2.01±0.01	1.9±0.3 4.1±0.3	3±1	0.60
21	Mo-$O_{(1)}$ Mo-$O_{(2)}$	1.74±0.01 2.01±0.01	1.8±0.2 4.1±0.2	3±1	0.35
22	Mo-$O_{(1)}$ Mo-$O_{(2)}$	1.76±0.01 2.03±0.02	1.6±0.3 4.1±0.3	3±1	0.56
23	Mo-$O_{(1)}$ Mo-$O_{(2)}$	1.76±0.01 2.03±0.01	1.8±0.3 4.2±0.3	3±1	0.55
24	Mo-$O_{(1)}$ Mo-$O_{(2)}$	1.76±0.01 2.03±0.01	1.7±0.3 4.3±0.3	3±1	0.62
25	Mo-$O_{(1)}$ Mo-$O_{(2)}$	1.75±0.01 2.03±0.01	1.6±0.3 4.3±0.3	3±1	0.49

Table S5 Fitted structure parameters using Mo K-edge EXAFS spectra of the *in situ* electrode before discharge, at the end of discharge, and with relaxation.

sample	Path	R (Å)	N	$\sigma^2\times10^{-3}$ (Å^2)	R factor (%)
Before discharge	Mo-O	1.75±0.01	4.1±0.5	6±2	0.59
End of discharge	Mo-O	1.76±0.01	1.4±0.3	3±1	0.45
	Mo-O	2.04±0.01	4.5±0.5	3±1	
	Mo-TM	2.61±0.02	6	25±3	
Relaxation	Mo-O	1.78±0.02	1.1±0.3	4±2	0.82
	Mo-O	2.05±0.01	4.2±0.6	4±2	
	Mo-TM	2.65±0.03	6	25±3	

Table S6 Fitted structural parameters of the Nb K-edge EXAFS spectra of the *in situ* electrode before discharge, at the end of discharge, and with relaxation.

sample	Path	R (Å)	N	$\sigma^2\times10^{-3}$ (Å^2)	R factor (%)
Before discharge	Nb-O	1.80±0.01	1.8±0.2	2±1	0.2
	Nb-O	1.97±0.01	1.2±0.3	2±1	
	Nb-O	2.13±0.01	3.0±0.1	2±1	
	Nb-TM	3.37±0.01	2	2±1	
	Nb-TM	3.53±0.01	2	2±1	
	Nb-TM	3.90±0.01	3	2±1	
	Nb-O	3.84±0.01	6	2±1	
	Nb-O-TM	3.86±0.03	2	3±1	
	Nb-O-O	3.11±0.01	8	3±1	
End of discharge	Nb-O	1.83±0.01	2.2±0.1	6±1	0.56
	Nb-O	2.02±0.01	3.1±0.2	6±1	
	Nb-TM	2.78±0.01	1	9±1	
	Nb-Li	2.98±0.01	6	12±1	
	Nb-Li	4.25±0.01	10	6±1	
	Nb-TM	3.34±0.01	2	6±1	
	Nb-O	3.74±0.01	4	6±1	
	Nb-O-TM	3.78±0.01	2	6±1	
	Nb-O-TM	3.89±0.01	4	6±1	
Relaxation	Nb-O	2.05±0.01	6.0±0.4	12±1	1.64
	Nb-TM	2.79±0.01	2	12±1	
	Nb-Li	2.80±0.02	6	12±1	
	Nb-TM	3.70±0.01	1	10±2	
	Nb-O-TM	3.96±0.01	2	10±2	

Supplementary References

[1] K.-D. Liss, B. Hunter, M. Hagen, T. Noakes, S. Kennedy, *J. Phys. B* **2006**, *385*, 1010.

[2] B. H. Toby, R. B. Von Dreele, *J. Appl. Crystallogr.* **2013**, *46*, 544.

[3] K. Momma, F. Izumi, *J. Appl. Crystallogr.* **2008**, *41*, 653.

[4] B. Ravel, M. Newville, *J. Synchrotron Radiat.* **2005**, *12*, 537.

[5] H. Idriss, *Surface Science* **2021**, *712*, 121894.